WILEY-VCH

DOI: 10.1002/ ((please add manuscript number))
Article type: Full Paper

Humidity-driven mechanical and electrical response of graphene/cloisite hybrid films

Rachele Castaldo†, Giuseppe Cesare Lama†, Paolo Aprea, Gennaro Gentile, Veronica Ambrogi*, Marino Lavorgna, Pierfrancesco Cerruti*

† These authors contributed equally to this work

Rachele Castaldo, Gennaro Gentile*, Pierfrancesco Cerruti
Institute for Polymers, Composites and Biomaterials, National Research Council of Italy, Via Campi Flegrei 34, 80078 Pozzuoli, Italy
E-mail: gennaro.gentile@cnr.it

Giuseppe Cesare Lama, Paolo Aprea, Veronica Ambrogi*
Department of Chemical, Materials and Production Engineering, University of Naples, Piazzale Tecchio 80, 80125 Napoli, Italy
E-mail: ambrogi@unina.it

Marino Lavorgna
Institute for Polymers, Composites and Biomaterials, National Research Council of Italy, P.le E. Fermi 1, 80055 Portici, Italy

Keywords: graphene/cloisite hybrids, reversible bending, humidity sensing, humidity-triggered actuators

Abstract. Humidity-driven and electrically responsive graphene/cloisite hybrid films are obtained by casting water dispersions of graphene oxide and cloisite Na^+. The hybrids are designed to exploit hydrophilicity and high water vapor barrier of the components. Coupling these properties in a homogenous film enables the realization of humidity-driven actuators, by generating a water gradient across the film section under asymmetric exposure to humidity. The hybrid films are self-standing, flexible and exhibit fast humidity-triggered bidirectional bending up to 75°, which is tuned by varying the relative amount of the two components. Up to 60% of the bending angle can be preserved at the steady state, providing a large and reliable response to humidity. Moreover, thermal treatment results in the reduction of graphene oxide, and the films show humidity-dependent electrical conductivity, with a progressive surface conductivity increase from about $1.5 \cdot 10^{-6}$ S at 20% RH up to $2.7 \cdot 10^{-5}$ S at

90% RH. The films are used to realize a humidity-sensitive electrical switching system in which the reversible actuation is due to water desorption induced by Joule effect. Due to their ease of preparation and tunable properties, this new class of graphene-based materials is suitable for the realization of humidity-driven and electrically responsive actuators and sensors.

1. Introduction

The design of bio-inspired systems, able to change their shape or properties in response to different external stimuli, such as changes of pH [1], temperature and light irradiation [2,3,4], electrical pulses [5] and water content [6], is attracting a large interest for the realization of smart systems, with high potentiality for application as sensors or actuators.

Different smart actuating materials, able to convert the energy applied through physical stimuli into macroscopic shape changes, have been described in recent literature. The first investigated systems mainly showed unidirectional bending actuation [7], whereas, more recently, different bidirectional bending actuators have been reported [8].

So far, actuating systems have been mainly designed by exploiting different properties of at least two different materials, either organic, inorganic or more recently biological, combined in multilayer membranes or films. For instance, the actuation under light irradiation of a bilayer membrane constituted by coupling a plain PDMS layer with a composite PDMS/graphene nanoplatelets layer has been explained by the differences in thermal expansion coefficient and Young's modulus of the two layers [4]. In another case, thermally-triggered shape-memory actuators have been realized through multilayer polymer structures constituted by glassy thermoset films anchored to pre-programmed liquid-crystalline films [9,10].

More specifically, several multilayered structures have been demonstrated able to respond to humidity variations. For instance, self-locomotive hygroscopically responsive structures have

been realized with aligned polyethylene oxide nanofibers electrospun on a silicon-based adhesive/polyimide layer [11]. Bilayer membranes prepared by sequential filtration of clay and graphene oxide dispersions have shown high and fast responsiveness to humidity and their bending has also been found triggered by vapors of alcohols, tetrahydrofuran, ethyl acetate, dichloromethane and acetone [12]. Microbial-based multilayer structures constituted by a biohybrid film obtained by *Escherichia coli* cells deposited on natural latex sheets have also shown humidity-triggered bending capability [13]. For all these systems, the humidity-driven bending mechanism is due to the large expansion/shrinking of a hygroscopically active layer as a function of the amount of absorbed/desorbed water, in comparison to the unresponsiveness to humidity of a hygroscopically inactive layer.

Nevertheless, producing multilayer structures is not the only possible approach for the realization of humidity-driven reversible actuators. Indeed, very recently, reversible bending induced by moisture has been observed in graphene oxide (GO) films obtained by vacuum filtration [14] as well as in monocomponent cellulose nanofiber films [15]. For both these systems, the formation of a bilayer-like structure of the film, obtained by anisotropic exposure to water vapor, is responsible for their bending. In fact, asymmetric exposure to humidity induces the creation of a water concentration gradient across the film, which generates a tensile stress gradient, inducing the film bending.

Starting from the available literature data, we supposed that a relevant factor for the actuation performance of homogeneous hydrophilic films should be their relatively high barrier to water vapor, which contributes to create high tensional states across the film, thus generating a high bending moment, until a steady state is obtained. Indeed, concerning the examples of monocomponent systems above reported, the barrier properties of GO towards several gases have been widely investigated [16]. For the system obtained by cellulose nanofibers, it must be underlined that, in comparison to paper-like materials constituted by cellulose fibers with micrometric diameter, cellulose nanofiber coatings show a strong reducing effect on water

vapor diffusion due to their high entanglements and swelling constraints of the rigid nanofiber network [17,18]. Furthermore, another polysaccharide-based system with interesting gas barrier properties has been recently reported as multi-responsive bidirectional bending actuator [19].

On these bases, we have hypothesized that humidity-driven bending capability of single-layer films can be modulated by realizing hybrid systems constituted by hydrophilic precursors with suitable water vapor barrier properties. Hydrophilicity is required to generate hygro-expansion, whereas low water vapor permeability is needed to enhance the bending moment. Therefore, in this paper we have designed new hybrid systems obtained by a facile evaporation casting of water dispersed mixtures of GO and cloisite, as both these materials show hydrophilic behavior as well as well documented water vapor barrier properties [19,20,21]. The structure and the humidity-triggered bidirectional bending of the obtained films were investigated, in view of modulating their properties varying the relative amount of the two components. Furthermore, upon mild thermal reduction, flexible reduced graphene oxide (rGO)/cloisite hybrids were obtained and their electrical conductivity was evaluated as a function of the relative humidity of the environment. Overall results have shown that, due to their ease of preparation and tunable properties, this new class of graphene/cloisite hybrids is suitable for applications as humidity-triggered actuators and humidity sensors.

2. Results and discussion

2.1. Cloisite and graphene-based hybrid films: structural and mechanical properties

Free-standing films with humidity-driven bending capability, with thickness ranging from 10 to 20 μm, were obtained by mild sonication of cloisite Na^+ (CNa) and GO water dispersions followed by casting (Figure 1a). The composition of the hybrid films was confirmed by thermogravimetric analysis (TGA) (Figure S1). Interestingly, the hybrid films showed

increased flexibility (Figure 1b) with respect to the fragile, monocomponent CNa and GO films that would easily break during handling.

SEM analysis was carried out on surfaces (Figures 1c-e) and cross sections (Figures 1f-h) of CNa, CNa/GO 50/50 and GO film. The surface of the CNa monocomponent sample showed the presence of numerous small wrinkles, while the cross section was characterized by a loosely packed arrangement of wavy silicate layers. On the other hand, GO film exhibited a smoother surface with few and larger wrinkles, and a more compact and well-stacked multilayered structure. The CNa/GO 50/50 hybrid film showed a highly corrugated surface due to the presence of large wrinkles, and an intermediate cross section morphology, suggesting an effective mixing of GO and CNa, and the consequent formation of an interconnected network. EDX mapping performed on surface (Figure S2) and cross-section (Figure 1i-k) of the hybrid CNa/GO 50/50 showed substantial film homogeneity, as proven by the similar distribution of carbon and silicon through the film section [22,23].

In order to impart electrical conductivity to the humidity-sensitive hybrids, rGO, CNa/rGO 50/50 and CNa/rGO 80/20 were prepared by thermal reduction of the parent GO-based samples [24]. The resulting films were observed by SEM (Figure S3), which evidenced that the thermal treatment induced the formation of smoother, less wrinkled surfaces with respect to the corresponding GO based films, especially in the case of graphene-rich samples (rGO and CNa/rGO 50/50).

The interaction between GO and CNa, as well as the effect of the thermal reduction process, were also investigated in terms of interlayer distance (d-spacing) and thickness of stacked GO and cloisite. To this purpose, XRD analysis was performed on CNa and pristine and reduced GO, CNa/GO 50/50 and CNa/GO 80/20. From XRD patterns (Figure 2a-b) the d-spacing of the GO and cloisite layers were evaluated, and the mean size of the domains stacked along the direction perpendicular to the film surface was calculated using the Debye-Scherrer equation [23**Errore. Il segnalibro non è definito.**]. Results are reported in Table 1. In the hybrid films,

an appreciable increase of GO interlayer distance from 0.823 nm to about 0.860 nm was observed for both the hybrid samples (Figure 2a), probably due to the interactions between the Na^+ cations of cloisite and the negatively charged surface of GO [25]. Moreover, the domain size of stacked GO in the CNa/GO 50/50 sample was noticeably smaller (6.2 nm) than that in pure GO (11.4 nm), which indicates that CNa reduced the tendency of GO to restack during water casting. Further increasing the cloisite content (sample CNa/GO 80/20) induced the opposite effect, as the mean size of the stacked GO layers raised to about 12.0 nm, likely due to GO phase segregation.

On the other hand, GO did not induce significant changes on the interlayer distance of cloisite lamellae, which remained almost constant at about 1.20 nm [26], but it influenced their mean size, which changed from about 8.2 nm (CNa) to 6.9 nm (CNa/GO 80/20) and to 4.5 nm (CNa/GO 50/50). It is worth to note that both cloisite and GO domains sizes were reduced by about 45 % in the hybrid CNa/GO 50/50 film, revealing that a high level of interactions was obtained in the equi-composition sample, as a consequence of hydrogen bonding between GO carboxyl groups and cloisite hydroxyl groups. Moreover, in aqueous dispersion, sodium cations acted as linkers between negatively charged GO and CNa surfaces [27,28]. Indeed, as revealed by ζ-potential measurements (Figure S4), GO and CNa both showed negative surface charge in aqueous dispersions.

The thermal reduction process caused a dramatic decrease of the rGO d-spacing (0.380 nm), confirming the formation of a graphite-like structure, and a large broadening of the corresponding XRD peak (Figure 2b), due to the decrease of the mean size of the stacked rGO layers to about 1.4 nm. In the hybrids, CNa inhibited restacking of rGO, increasing the interlayer distance (0.589 nm for CNa/rGO 50/50 and 0.500 nm for CNa/rGO 80/20). In these cases, a significant broadening of the XRD peak attributed to the rGO component was also observed, whereas the average domain size was not determined, due to the very low intensity of these peaks.

Concerning cloisite, thermal reduction did not induce significant changes on the d-spacing, however the mean size of the domains decreased to the lowest values, about 3.1 and 3.4 nm for CNa/rGO 50/50 and CNa/rGO 80/20, respectively, which indicates that the restacking during GO reduction induced a further size decrease of the cloisite domains.

The effect of the thermal reduction of GO was also evaluated by EDX analysis, which revealed that C/O atomic ratio increased from 1.28 ± 0.06 for GO to 2.91 ± 0.12 for rGO. Moreover, Raman spectroscopy analysis (Figure S5) was also performed on pristine and thermally treated GO and CNa/GO 50/50. By spectral deconvolution, it was found that the thermal reduction did not significantly affect the I_D/I_G ratio, which was about 0.92 for all samples, irrespectively of the composition and the thermal reduction process. EDX and Raman results were consistent with the mild thermal reduction conditions selected to preserve the good mechanical properties and the flexibility of the reduced rGO and CNa/rGO samples. Indeed, mechanical properties of pristine and reduced films were evaluated by tensile tests (see Figures 2c-d and Table 1). Interestingly, GO and CNa had a synergistic effect on the mechanical performance of hybrid films, which showed elongation and stress at break values twice as high as monocomponent GO and CNa films. On the other hand, the Young's modulus (E) of CNa/GO 50/50 and CNa/GO 80/20 resulted intermediate between GO and CNa showing about 20% and 30% reduction, respectively, compared to GO. Consistently with data reported in literature on rGO films, [29] the thermal reduction had a detrimental effect on the Young's modulus of rGO. Nonetheless, the presence of cloisite contributed to preserve the mechanical properties of the hybrids.

An interesting feature of GO, cloisite and GO/CNa hybrid films is their ability to undergo expansion/contraction phenomena if exposed to controlled and cyclic humidity variations, acting as humidity-driven tensile actuators. Contractile stress curves of CNa, pristine and reduced GO, CNa/GO 50/50 and CNa/GO 80/20 during consecutives 0.7% - 5.7% RH cycles were recorded (Figure 2e-f). GO displayed the highest contractile stress, reaching 5.4 MPa by

decreasing RH from 5.7 to 0.7%. In the same conditions, CNa, CNa/GO 80/20 and CNa/GO 50/50 contractile stresses reached respectively 4.7 MPa, 4.4 MPa and 3.7 MPa. The same tests performed on the thermally reduced samples showed a decrease of the maximum contractile stress, which was more evident for the samples containing more GO phase. Indeed, rGO stress was more than 50% lower than that of GO, while a slight reduction was noticed for CNa/rGO 50/50 and CNa/rGO 80/20 with respect to the corresponding pristine samples. Furthermore, cyclic degassing was performed on pristine GO, CNa, CNa/GO 50/50 and CNa/GO 80/20, changing the test chamber conditions from 5.7% RH to a dry state (high vacuum, $P = 1.3 \cdot 10^{-3}$ Pa) and then again to 5.7% RH. This procedure resulted in a remarkably enhanced contractile stress, which ranged from about 7 to 10 MPa (Figure S6). These values are on average lower than those recorded for GO/polyvinylidene fluoride bilayer actuators (8 MPa from 43% to a fully wet state) [30] and polypyrrole/polyol-borate films (27 MPa from the fully wet to the fully dry state) [6]. However, the latter were investigated imposing much larger RH changes. Comparing the expansion/contraction behaviour of the CNa/GO hybrid systems with the results gained by tensile stress-strain curves (Figure 2) indicated that, in the selected humidity conditions, all the samples worked in elastic regime. Indeed, for all the samples, an almost complete relaxation occurred in about 200 s during the RH increase step from 0.7 to 5.7% RH, and in about 400 s from high vacuum regime to 5.7% RH. Nonetheless, in some cases a small residual contractile stress was recorded, especially for the samples showing higher contractile stresses.

2.2. Humidity-driven bending actuators based on GO hybrids

Water wettability of pristine and reduced films was evaluated through surface contact angles (CA) measurements (Figure S7 and Table 1). CNa film showed an average CA of 50°, while GO contact angle was about 73°, and reached 80° upon reduction (rGO). CA values of the hybrid films were considerably lower (37° and 39° for CNa/GO 50/50 and for CNa/GO 80/20,

respectively), showing a more hydrophilic surface, which was expected to enhance the bending ability. This decrease of the contact angle value with respect to the monocomponent GO and CNa films can be explained by considering the corrugated surface evidenced by the hybrid films, as shown in Figures 4d and 4g. Indeed, according to the Wenzel model, for CA values lower than 90°, as those evidenced for both CNa and GO, an increase of the surface roughness decreases the contact angle [31]. Moreover, upon thermal reduction, the contact angle of the hybrid films significantly increased, reaching the value of about 80° for both CNa/rGO 50/50 and CNa/rGO 80/20.

Qualitative assessments of the bending capability of GO, CNa and hybrid films indicated that all of them quickly deflected upward (within seconds) once placed on a bare palm, whereas they did not bend when placed on dry substrates. The bending is well explained by a difference of relative humidity between the two sides of the film, which generates a bilayer-like structure in terms of moisture gradient induced in the direction perpendicular to the film surfaces [14,15]. A schematic representation of this phenomenon is depicted in Figure 3a, where a hybrid film section is constituted by orange and black rectangles, representing respectively CNa and GO platelets. Indeed, the asymmetrical exposure of the film to humidity induces the expansion of the lower part of the film, generating corresponding compression stresses in the upper one. These expansion/compression stresses generate a bending moment on the film, inducing the upward deflection.

The kinetics of this humidity-driven bending actuation was evaluated for the CNa/GO 50/50 hybrid. A rectangular-shaped film of CNa/GO 50/50 was positioned on a metallic grid, which was placed on a petri dish containing water. As shown in the image sequence in Figure 3b1-8 and in the diagram in Figure 3c, the film, when exposed to asymmetrical moisture, suddenly deflected upward, reaching the maximum bending extent of about 50° within 30 s. This bending actuation is driven by the formation of a steep humidity gradient across the film. A schematic representation of the kinetics of the water gradient across the film section is

reported in Figure 3d. As sketched, eventually the water gradient get progressively smoother, evolving towards the equilibrium linear profile, thus inducing a decrease of the sample deflection. For CNa/GO 50/50, in these conditions, equilibrium was reached after 1 day of asymmetrical humidity exposure, and the film showed an ultimate and constant deflection angle of about 30°.

This humidity-driven bending is fully reversible, as the films recovered their original flat shape upon removal of the moisture source. Moreover, when the bent films were turned upside down, curvature was reversed in less than 3 seconds, demonstrating the bi-directionality of the humidity-driven deflection. This phenomenon is demonstrated by the series of photographs collected in Figures 3e. A CNa/GO hybrid film exposed to humidity with the bottom side deflects upward and, after being turned upside down (between Figures 3e2 and 3e3), it changes its curvature, first assuming a flat position, and then deflecting upward again (Figures 3e4 to e6).

The bending extent of GO, CNa and CNa/GO hybrid films was evaluated as a function of the composition of the films. To this purpose, rectangular-shaped GO, CNa and hybrid films were clamped on one end and placed above a Petri dish containing water, in a climatic chamber at 50% RH. The bending angle (β) (Figure 4b) was evaluated by image analysis on digital pictures collected 30 s after placing the Petri dish underneath the film. GO and CNa showed maximum bending angles of 13° and 34°, respectively. The value observed for GO was lower with respect to the data reported in literature [14], due to the lower operating temperature and to the larger thickness of our films. Increasing contents of CNa in the hybrid systems induced a remarkable increase of bending, as CNa/GO 20/80 and CNa/GO 40/60 showed bending angles of about 40 and 35°, respectively. With the same experimental setup, the best performance was achieved by CNa/GO 50/50, which reached a bending angle of 75°. A further increase of CNa brought about a reduction of the deflection angle, which decreased to values close to those observed for plain CNa.

To elucidate the humidity-driven bending behavior, water vapor permeability and water absorption tests were carried out on GO, CNa and the hybrids samples CNa/GO 50/50 and CNa/GO 80/20. Permeability tests provided an interesting trend, as CNa/GO 50/50 film showed the lowest permeability of $2.4 \cdot 10^{-11} \pm 4.2 \cdot 10^{-14}$ g/(Pa s m), followed by CNa/GO 80/20, $2.8 \cdot 10^{-11} \pm 1.0 \cdot 10^{-12}$ g/(Pa s m), CNa, $3.0 \cdot 10^{-11} \pm 1.2 \cdot 10^{-12}$ g/(Pa s m), and GO, $3.5 \cdot 10^{-11} \pm 4.8 \cdot 10^{-13}$ g/(Pa s m). Water absorption tests revealed a water uptake between 16 and 17 wt% for all samples. Therefore, all samples have similar water solubility, and the permeability reduction must be attributed to a diffusivity decrease. Most likely, the increase of barrier properties is correlated to strong GO/CNa interactions, which are maximized in the CNa/GO 50/50 film, as also demonstrated by XRD results. Indeed, the reduction of GO and cloisite domains size in CNa/GO 50/50 film plays a key role in obstructing the water vapor diffusion through the hybrid film. The diffusion and permeability decrease, in turns, generates in CNa/GO 50/50 a high water gradient when the film is exposed to asymmetrical moisture, thus enhancing the humidity-driven bending extent.

Due to its outstanding bending actuation, CNa/GO 50/50 was selected to test the response to repeated asymmetric exposure to moisture. For this purpose, the bending experiment was performed in three consecutive cycles, each consisting in moving the film away from the water-containing Petri dish after 40 s and re-exposing it to the moisture-source once it recovered its original flat shape (see Figures 4a4 and 4b and Supplementary Video 1). As shown, a decrease of the recorded bending angle was observed during successive cycles (β = 75° in the 1st cycle, 70° in the 2nd cycle and 61° in the 3rd one). This effect indicates a progressive saturation of the film with water, due to the fast re-exposure to moisture, which does not allow the material to fully desorb the water molecules adsorbed during the previous cycle. Qualitative assessments of the bending actuation of the samples based on rGO indicated that comparatively smaller bending angles were generated by asymmetric moisture exposure, due to their reduced water absorption capacity.

2.3. Humidity-driven electrical-responsive sensors and actuators

Although the reduction of the GO-containing samples had a detrimental effect on the bending actuation, rGO enhanced electrical conductivity of hybrid films, allowing their potential application as humidity sensors and actuators. [32] Preliminary resistivity measurements showed that GO-based hybrid films presented surface electrical resistivity comparable to that of CNa (~ 10^8 Ω/sq) while, upon thermal reduction, the surface resistivity decreased by about two orders of magnitude. Therefore, CNa/rGO 50/50 was selected to evaluate its electrical response under humidity-controlled conditions. To this purpose, a CNa/rGO 50/50 rectangular-shaped film was clamped to an electrode at one end and placed above a Petri dish containing water, at room temperature, likewise the bending experiment reported in Section 2.2. In addition, the other electrode was placed above the CNa/rGO 50/50 film at a distance of 7 mm, ensuring that the right end of the electrode and the left end of the film overlapped (see scheme in Figure 5a). Once the CNa/rGO 50/50 film was asymmetrically exposed to moisture, it deflected upward and touched the lower surface of the upper electrode, thus closing the electrical circuit set at 3V DC voltage. The current passing in the circuit induced a Joule heating effect, which promoted water desorption and consequently triggered the relaxation of the film and the opening of the electrical circuit. The Joule heating of the sample was confirmed using a thermal camera (Supplementary Video 2 and Figures 5b-c), which showed that in the closed circuit CNa/rGO 50/50 (in orange, Figure 5b) had a temperature of about 2-3 °C higher than that recorded in the open circuit (in blue, Figure 5c). This experiment was performed in a chamber at 40% RH, so the CNa/rGO 50/50 film resulted exposed to about 60% RH gradient. This means that, by changing the distance between the film in the flat shape and the electrode above the Petri dish and taking advantage of the bending capability of the CNa/rGO hybrid films, it is possible to design humidity sensors/actuators which respond to specific relative humidity gradient values.

The effect of CNa on the electrical response of the reduced hybrid films in controlled humidity conditions was also evaluated. Therefore, the surface conductivity (σ_S) of CNa/rGO 50/50 and CNa/rGO 80/20 films was measured at RH values ranging from 20% to 90%. The electrical response registered demonstrated that for both films σ_S increases with RH. This phenomenon is ascribed to CNa ionic conductivity, which increases when adsorbed water molecules intercalate between CNa lamellae, improving the mobility of Na^+ ions [33]. Indeed, CNa/rGO 80/20 was more sensitive to humidity (Figures 5d-f), providing increased conductivity with respect to CNa/rGO 50/50 as a function of RH. More in details, for humidity values ranging from 20 to 60%, CNa/rGO 50/50 did not show significant differences in the electrical conductivity, while from 70% RH on, the σ_S dependence on RH became significant. CNa/rGO 80/20, on the other hand, exhibited much more exploitable humidity sensing properties, since its conductivity monotonically increased with RH in the range 20-90%. In particular, the sensor showed moderate sensitivity to moisture up to 50% RH (Figure 5f) while, above this value, the sensitivity of the RH sensor progressively improved, showing differences of surface conductivity up to $6.0 \cdot 10^{-4}$ S between 87 and 90% RH. In these conditions, the current intensity circulating in the 3V circuit was high enough to induce an appreciable Joule heating effect, responsible for the partial desorption of water from the film. Consequently, the ionic conductivity induced by CNa was reduced, leading to a decrease of the conductivity in the early 10s of measurements, followed by a plateau. This behavior did not preclude the sensor performances, as the plateau conductivity signals recorded at different RH values were well separated and never overlapped. Noteworthy, the surface conductivity stationary values of both CNa/rGO 50/50 and CNa/rGO 80/20 at variable RH are well fitted with an exponential function, whose calculated fitting parameters are reported in Figure 5f.

3. Conclusions

New self-standing hybrid films are developed by facile mixing and casting of water dispersed graphene oxide and cloisite. Unlike fragile monocomponent graphene oxide or cloisite films, the hybrids show outstanding flexibility and improved mechanical properties. The coexistence of both graphene oxide and cloisite induces a pronounced humidity-triggered bidirectional bending of the films upon asymmetric exposure to moisture. The bending extent, which in our experimental conditions reached angles up to 75°, can be modulated by varying the relative amount of the components. Up to 60 % of the bending angle is preserved at the steady state, providing a large and prolonged response to humidity.

By mild thermal reduction, flexible reduced graphene oxide/cloisite hybrids are obtained. These systems showed a humidity-dependent electrical conductivity, with an exponential increase of the measured surface conductivity from about $1.5 \cdot 10^{-6}$ S at 20% RH up to $2.7 \cdot 10^{-5}$ S at 90% RH. The sensing/actuation capability of these hybrid films was demonstrated through the set-up of a humidity sensitive electrical switching system in which, under asymmetric exposure to moisture, a flat film bends and gets in contact with an electrode, closing an electric circuit. Heated by Joule effect, the bent film releases water and recovers its original flat shape.

Due to their facile preparation and tunable properties, this class of graphene/cloisite hybrids represents the basis for the development of new humidity-driven mechanically and electrically responsive actuators and sensors.

Experimental Section

Materials: Graphene oxide water dispersion (4.5 g/L) was purchased from Nanesa S.r.l. (Arezzo, Italy). Cloisite Na^+ was purchased from BYK-Chemie GmbH (Wesel, Germany).

Preparation of CNa/GO films: Hybrid films made of graphene oxide (GO) and cloisite Na^+ (CNa) were prepared by water evaporation from mixed CNa/GO water dispersions. CNa was dispersed in distilled water at 4.5 mg/mL concentration by sonication with a Sonics Vibracell

ultrasonic processor (500 W, 20 kHz), at 25% of amplitude for 30 min, with 30s/30s on/off cycles. Then, proper amounts of CNa dispersion were poured into the GO dispersions in order to obtain 5 mixtures with the following CNa/GO weight ratios: 20/80, 40/60, 50/50, 60/40, 80/20. These dispersions were sonicated for 15 minutes with 30s/30s on/off cycles and then poured in petri dishes to obtain CNa/GO films with 10-20 μm thickness upon water evaporation. Petri dishes were kept on a levelled laboratory bench at room temperature until complete drying, which occurred in about 60 hours. The cast films were labeled as CNa/GO 20/80, CNa/GO 40/60, CNa/GO 50/50, CNa/GO 60/40, CNa/GO 80/20. For comparison, GO and CNa dispersions were processed in the same way to prepare plain GO and CNa films. Thermally reduced films of GO, CNa/GO 50/50 and CNa/GO 80/20 were prepared through the same procedure, followed by a 180 °C thermal treatment in oven for 2 hours. Obtained films were coded as rGO, CNa/rGO 50/50 and CNa/rGO 80/20.

Characterization techniques: CNa, pristine and reduced GO, CNa/GO 50/50 and CNa/GO 80/20 films surfaces were observed by scanning electron microscopy (SEM) with a FEI Quanta 200 FEG SEM in high vacuum mode. Before SEM observations, the samples were mounted onto SEM stubs by means of carbon adhesive disks and sputter coated with a 5-10 nm thick Au-Pd layer. All the samples were observed at 10-20 kV acceleration voltage using a secondary electron detector. CNa, GO, and CNa/rGO 50/50 cross-sections were observed in the same way.

Energy dispersive X-ray (EDX) mapping analysis was performed on the CNa/GO 50/50 film surface and cross-section by means of a FEI Quanta 200 FEG SEM equipped with an Oxford Inca Energy System 250 and an Inca-X-act LN2-free analytical silicon drift detector. EDX analysis was also performed on GO and rGO surface to evaluate the C/O atomic ratio.

Zeta potential measurements were performed on GO and CNa 4.5 mg/mL dispersions by laser doppler micro-electrophoresis (LDME), using a Zetasizer Nano ZS (Malvern Instruments). Measurements were performed in triplicate at 25 °C.

Thermogravimetric analysis was performed on GO, CNa and hybrid films using a Mettler TGA/SDTA851 analyzer. All the samples were analyzed in oxidizing atmosphere at 10 °C/min heating rate, from 100 °C to 800 °C, using about 2 mg of material. Measurements were performed in triplicate.

A FTA 1000 (First Ten Ångstroms) instrument was used to measure static contact angles (CA) of CNa and pristine and reduced GO, CNa/GO 50/50, and CNa/GO 80/20 samples. The samples were attached on a double-sided tape applied on a microscope glass and a 1-μL distilled water droplet was positioned on the film surface. Each measurement was repeated on six different areas of the sample on the top and the bottom surface. The experiments were conducted at room temperature. CA was geometrically evaluated as the angle formed by the solid surface and the tangent to the droplet. Since CA values recorded on the upper and lower surfaces were very similar for all the films, reported data are the average of values measured on both the surfaces of each sample.

Wide-angle X-ray diffraction (XRD) analysis was carried out on CNa, pristine and reduced GO, CNa/GO 50/50 and CNa/GO 80/20 samples by means of a Panalytical X'Pert Pro diffractometer equipped with PixCel 1D detector using a Ni-filtered $CuK_{\alpha1}/K_{\alpha2}$ radiation generated at 40 kV and 40 mA. To separate the individual components in unresolved XRD profiles, spectral deconvolution was performed with the software Grams/8.0AI, using Lorentzian functions. The d-spacing (d_i) of CNa and GO layers and the average size (D_i) of CNa and GO stacked domains in the direction perpendicular to the plane were calculated respectively applying the Bragg's law and the Debye-Scherrer equations to each reflection centered at $2\theta_i$ [23]. Confocal Raman spectra were acquired on GO, rGO, CNa/GO 50/50 and CNa/rGO 50/50 films by a Horiba-Jobin Yvon Aramis Raman spectrometer operating with a diode laser excitation source limiting at 532 nm and a grating with 1200 grooves/mm. The 180° back-scattered radiation was collected by an Olympus metallurgical objective (MPlan 50X, NA = 0.50) and with confocal and slit apertures both set to 400 mm. The radiation was

focused onto a Peltier-cooled CCD detector (Synapse Mod. 354308) in the Raman-shift range 3200–800 cm^{-1}. To separate the individual peaks in unresolved, multicomponent profiles, spectral deconvolution was performed using the above mentioned software Grams/8.0AI, using a Lorentzian function. By a curve fitting of the data, height, area and position of the individual components were calculated.

Tensile tests were performed on rectangular shaped samples (about 15 μm thickness, 6 mm width, 10 mm gauge length) of CNa, pristine and reduced GO, CNa/GO 50/50 and CNa/GO 80/20 in a FEI Quanta 200 FEG SEM, used as a test chamber, equipped with a Deben microtensile test apparatus. Stress strain curves were recorded with a 200 N load cell, setting the crosshead speed at 0.2 mm/min. Tests were performed in low vacuum mode, setting the water vapor pressure at 160 Pa and the temperature of 23 °C. The effect of the humidity changes on the contraction and relaxation of CNa, and pristine and reduced GO, CNa/GO 50/50 and CNa/GO 80/20 was evaluated using the above cited Deben microtensile test apparatus, programming in the test chamber 200 s cyclic 20 - 160 Pa water vapor pressure cycles, corresponding, at the temperature of 23°C, to 0.7 - 5.7% RH cycles. Pristine samples were also subjected to a high vacuum/low vacuum 400 s cycle, ranging from 160 to $1.3 \cdot 10^{-3}$ Pa.

The bending of GO, CNa and hybrid films exposed to humidity gradient was measured through a home-made set-up. In a climatic chamber (MMM Group, Climacell 770) set at 25 ± 0.1 °C and 50 ± 1% RH, rectangular shaped films, measuring 6 x 25 mm, 15 μm thickness, were fixed on a flipped-over Petri dish, letting 15 mm of the film end leaning out of the Petri. A water-containing Petri dish was positioned close to the flipped-over Petri dish, underneath the protruding film end. Therefore, the region of the film leaning out of the Petri resulted exposed to a 50 % humidity gradient. A camera was positioned in the chamber to register the bending of the film. The maximum bending angle of the film was measured as the maximum angle (β) formed by the film with the horizontal.

Swelling test were performed on CNa, GO and CNa/GO 50/50 films by gravimetrically determining the moisture absorption on film conditioned for 72 h hours at 50 % RH after vacuum drying for at least 24h.

Water vapor permeability was evaluated by means of a Multiperm apparatus (Extra Solution, Pisa, Italy) working in a gas/membrane/gas configuration, at 25 ± 1 °C and 50 ± 0.5% RH. The exposed area of the film was 2,01 cm^2.

A custom set-up aiming to exploit the sensing and actuating capability of the CNa/GO hybrid films was realized. For this experiment, a configuration similar to the bending test one was used. A CNa/rGO 50/50 film was connected to an electrode through copper tape and positioned on a flipped-over Petri dish. A second electrode (Electrode 2) was placed on another Petri dish (Petri 2) containing water and semi-covered with a barrier polypropylene sheet. In particular, a portion of the Petri 2 suitable to let the CNa/rGO 50/50 film lean over the water surface was left uncovered. After applying a 3V voltage between the electrodes, the dishes were brought close to each other. Electrode 2 was placed in a position so that the test film, when bending because exposed to a humidity gradient, would enter in contact with it. The experiment was performed at 23 °C and 40 %RH. The experiment was simultaneously recorded with a digital camera and an infrared thermal camera (FLIR Systems, Thermo Vision A40M).

Finally, surface resistivity measurements at different RH were performed on CNa/rGO 50/50 and CNa/rGO 80/20 films. Hybrid films, measuring 25 mm x 6 mm, 15 µm thickness, were connected with copper adhesive tapes to two multimeters, the first one (Keithley Electrometer/High resistance meter, Model 6517A) used to apply a 3 V voltage, and the other (Agilent 34401A Multimeter) to collect values of the direct current passing through the samples. The samples were placed in the climatic chamber set at 25 ± 0.1 °C and at relative humidity values ranging between 20 and 90 %. Before each measurement, the climatic chamber was set at the required relative humidity for two hours, allowing the sample

equilibrate with the ambient humidity. Then, the voltage was applied and intensity current measurements were taken for 120 s.

Supporting Information
Supporting Information is available from the Wiley Online Library or from the author.

Acknowledgements

Rachele Castaldo and Giuseppe Cesare Lama contributed equally to this work

Received: ((will be filled in by the editorial staff))
Revised: ((will be filled in by the editorial staff))
Published online: ((will be filled in by the editorial staff))

References

[1] X.-J. Han, Z.-Q. Dong, M.-M. Fan, Y. Liu, J.-H. li, Y.-F. Wang, Q.-J. Yuan, B.-J. Li, S. Zhang, *Macromol. Rapid Commun.* **2012**, *33*, 1055.

[2] X. Lu, S. Guo, X. Tong, H. Xia, Y. Zhao, *Adv. Mater.* **2017**, 29, 1606467.

[3] G. C. Lama, P. Cerruti, M. Lavorgna, C. Carfagna, V. Ambrogi, G. Gentile, *J. Phys. Chem. C* **2016**, *120*, 24417.

[4] W. Jiang, D. Niu, H. Liu, C. Wang, T. Zhao, L. Yin, Y. Shi, B. Chen, Y. Ding, B. Lu, *Adv. Funct. Mater.* **2014**, *24*, 7598.

[5] P. Chen, Y. Xu, S. He, X. Sun, W. Guo, Z. Zhang, L. Qiu, J. Li, D. Chen, H. Peng, *Adv. Mater.* **2015**, *27*, 1042.

[6] M. Ma, L. Guo, D. G. Anderson, R. Langer, *Science* **2013**, *339*, 186.

[7] Y. Hu, T. Lan, G. Wu, Z. Zhua, W. Chen, *Nanoscale* **2014**, *6*, 12703.

[8] M. Weng, P. Zhou, L. Chen, L. Zhang, W. Zhang, Z. Huang, C. Liu, S. Fan, *Adv. Funct. Mater.* **2016**, *26*, 7244.

[9] A. Belmonte, G. C. Lama, G. Gentile, P. Cerruti, V. Ambrogi, X. Fernández-Francos, S. De la Flor, *Eur. Polym. J.* **2017**, *97*, 241.

[10] A. Belmonte, G. C. Lama, P. Cerruti, V. Ambrogi, X. Fernández-Francos, S. De la Flor, *Smart Mater. Struct.* **2018**, *27*, 075013.

[11] B. Shin, J. Ha, M. Lee, K. Park, G. H. Park T. H. Choi, K.-J. Cho, H.-Y. Kim, *Sci. Robot.* **2018**, 3, eaar2629.

[12] R. K. Gogoi, K. Saha, J. Deka, D. Brahma, K. Raidongia, *J. Mater. Chem. A* **2017**, *5*, 3523.

[13] W. Wang, L. Yao, C.-Y. Cheng, T. Zhang, H. Atsumi, L. Wang, G. Wang, O. Anilionyte, H. Steiner, J. Ou, K. Zhou, C. Wawrousek, K. Petrecca, A. M. Belcher, R. Karnik, X. Zhao, D. I. C. Wang, H. Ishii, *Sci. Adv.* **2017**, *3*, e1601984.

[14] Y. Ge, R. Cao, S. Ye, Z. Chen, Z. Zhu, Y. Tu, D. Ge, X. Yang, *Chem. Comm.* **2018**, *54*, 3126.

[15] M. Wang, X. Tian, R. H. A. Ras, O. Ikkala, *Adv. Mater. Interfaces* **2015**, *2*, 1500080.

[16] Y. Su, V. G. Kravets, S. L. Wong, J. Waters, A. K. Geim, R. R. Nair, *Nat. Comm.* **2014**, *5*, 4843.

[17] J. Wang, D. J. Gardner, N. M. Stark, D. W. Bousfield, M. Tajvidi, Z. Cai, *ACS Sust. Chem. Eng.* **2018**, *6*, 49.

[18] S. S. Nair, J. Y. Zhu, Y. Deng, A. J. Ragauskas, *Sust. Chem. Process.* **2014**, *2*, 23.

[19] T. Wang, M. Li, H. Zhang, Y. Sun, B. Dong, *J. Mater. Chem. C* **2018**, *6*, 6416.

[20] G. Scherillo, M. Lavorgna, G. G. Buonocore, Y. H. Zhan, H. S. Xia, G. Mensitieri, L. Ambrosio, *ACS Appl. Mater. Interfaces* **2014**, *6*, 2230.

[21] B. Tan, N. L. Thomas, *J. Membrane Sci.* **2016**, *514*, 595.

[22] C. Chen, Q.-H. Yang, Y. Yang, W. Lv, Y. Wen, P.-X. Hou, M. Wang, H.-M. Cheng, *Adv. Mater.* **2009**, *21*, 3007

[23] R. Castaldo, G. C. Lama, P. Aprea, G. Gentile, M. Lavorgna, V. Ambrogi, P. Cerruti, *Micropor. Mesopor. Mat.* **2018**, *260*, 102.

[24] K. Moon, J. Lee, R. S. Ruoff, H. Lee, *Nat. Comm.* **2010**, *1*, 73.

[25] A. Lerf, H. He, M. Forster, J. Klinowski, *J. Phys. Chem. B* **1998**, *102*, 4477–4482.

[26] A.R. Ramadan, A. M. K. Esawi, A. A. Gawad, *Appl. Clay Sci.* **2010**, 47,196.

[27] M. Darder, P. Aranda, C. Ruiz-García, F.M. Fernandes, E. Ruiz-Hitzky, *Adv. Funct. Mater.* **2018**, 28, 1704323.

[28] C. Zhang, W.W. Tjiu, W. Fan, Z. Yang, S. Huang, T. Liu, *J. Mater. Chem.* **2011**, 21, 18011.

[29] S. Pei, J. Zhao, J. Du, W. Ren, H.-M. Cheng, *Carbon* **2010**, *48*, 4466-4474.

[30] G. Xu, M. Zhang, Q. Zhou, H. Chen, T. Gao, C. Li, G. Shi, *Nanoscale* **2017**, *9*, 17465.

[31] D. Parobek, H. Liu, *2D Mater.* **2015**, 2, 032001.

[32] H. Bi, K. Yin, X. Xie, J. Ji, S. Wan, L. Sun, M. Terrones, M. S. Dresselhaus, *Sci. Rep.* **2013**, *3*, 2714.

[33] F. Salles, S. Devautour-Vinot, O. Bildstein, M. Jullien, G. Maurin, J. C. Giuntini, J.-M. Douillard, H. Van Damme, *J. Phys. Chem. C* **2008**, *112*, 14001-14009.

-

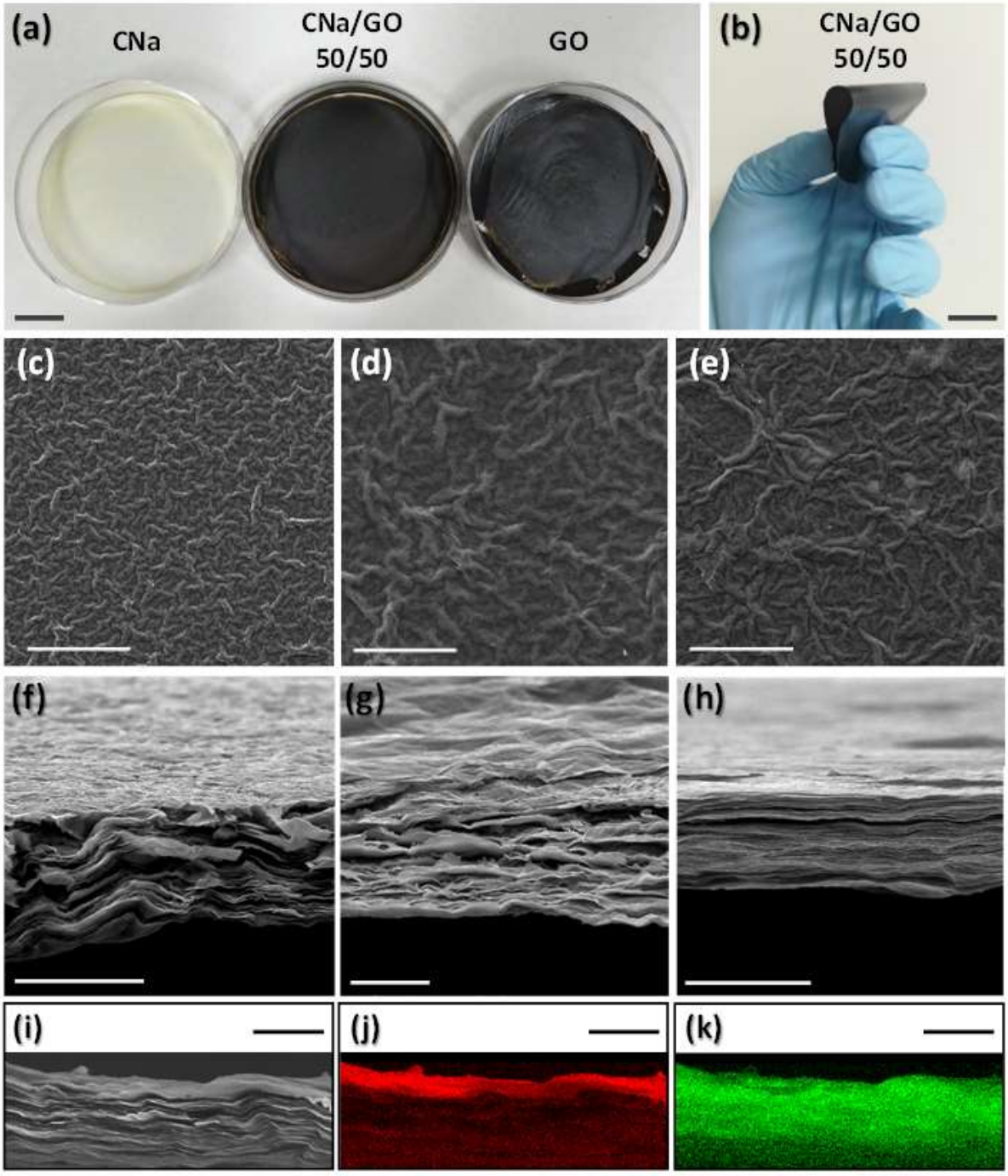

Figure 1. Images of CNa, CNa/GO 50/50 and GO cast films (a); scale bar 2 cm. Image of the CNa/GO 50/50 film (b). SEM images of upper surfaces of CNa (c), CNa/GO 50/50 (d) and GO (e); scale bar 100 µm. SEM images of sections of CNa (f), CNa/GO 50/50 (g) and GO (h); scale bar 10 µm. SEM image (i), carbon (j) and silicon (k) EDX maps of the CNa/GO 50/50 section; scale bar 5 µm.

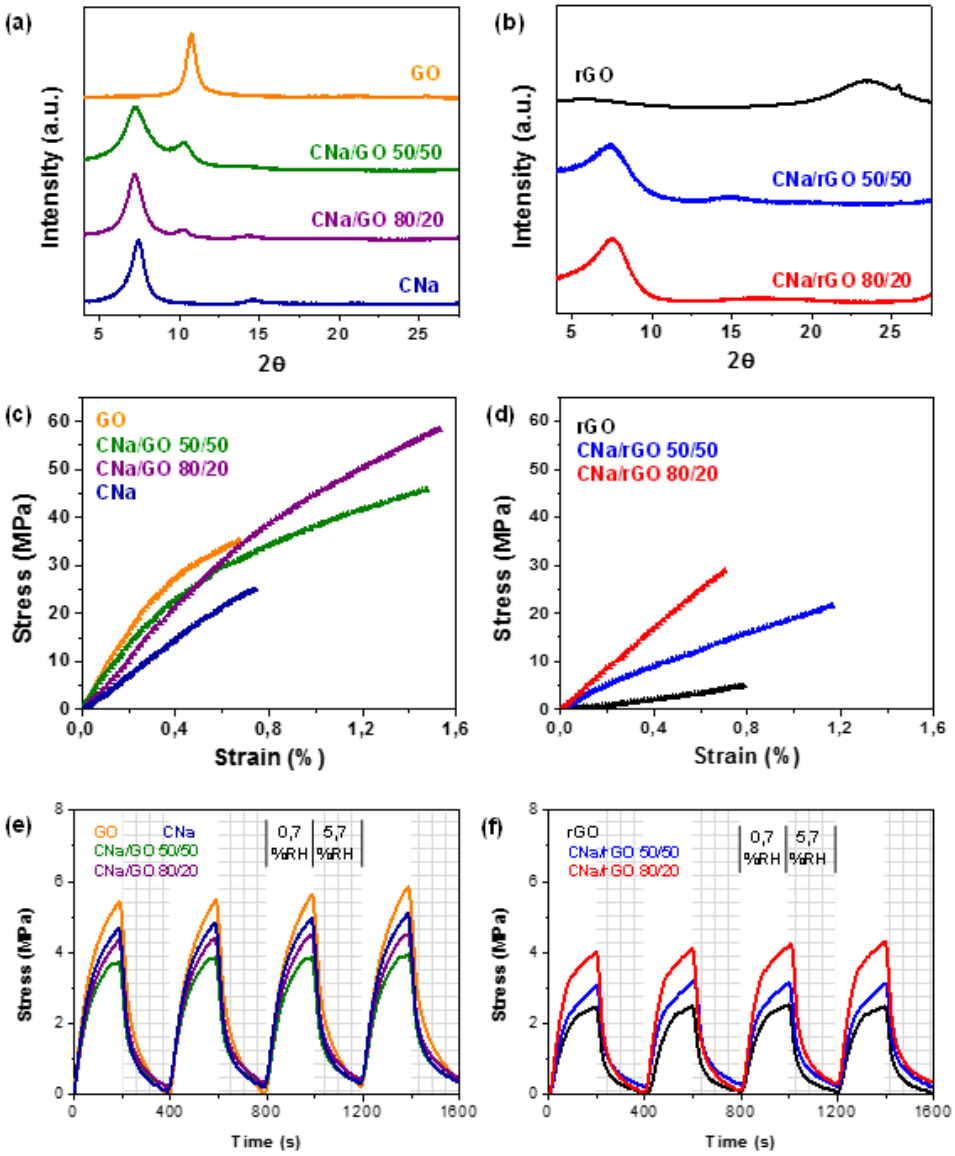

Figure 2. XRD spectra (a,b), stress-strain curves (c,d) and contractile stress curves during consecutives 0.7 % RH and 5.7 % RH cycles (e, f) of GO, CNa, CNa/GO 50/50, and CNa/GO 80/20 films and the corresponding thermally reduced samples.

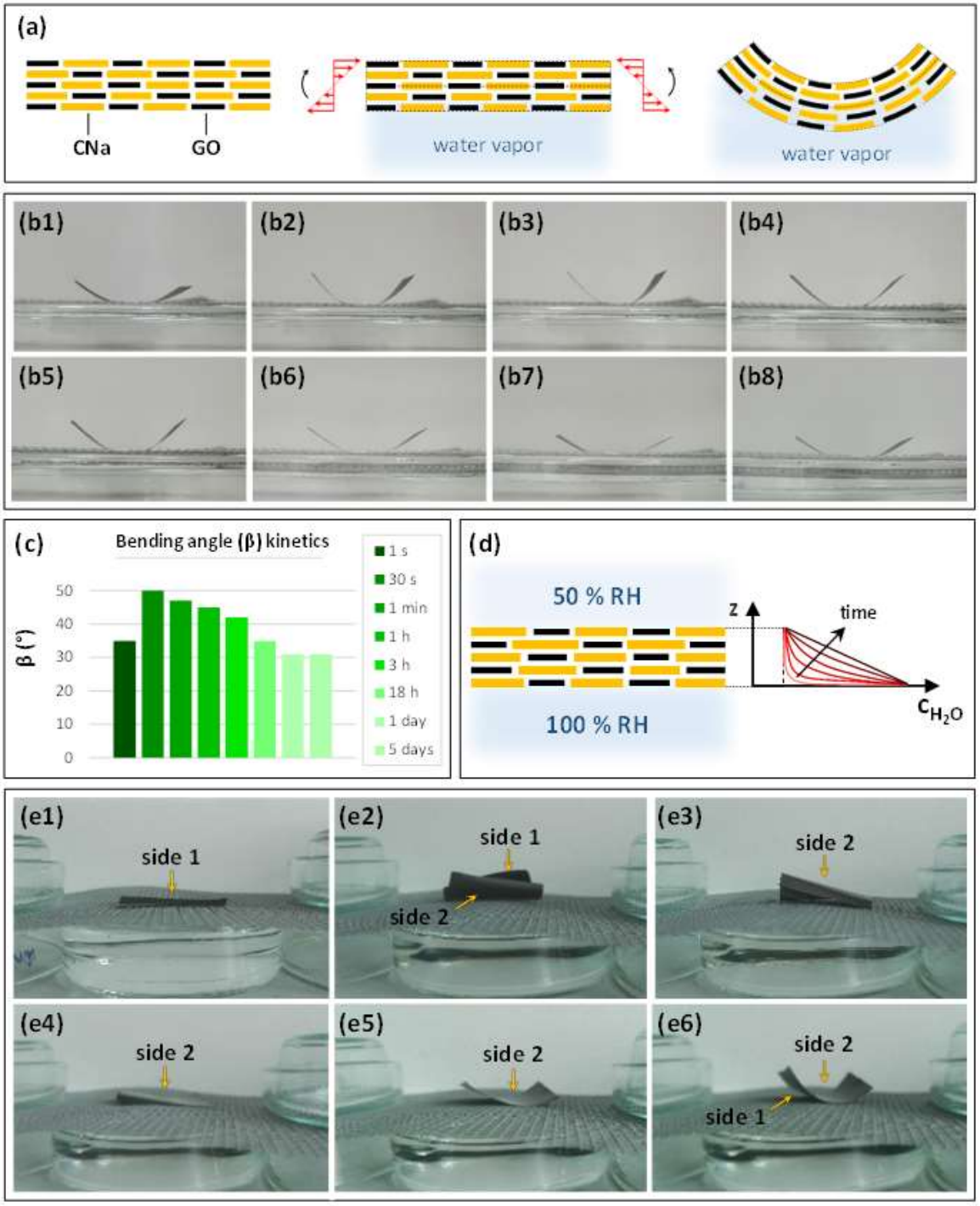

Figure 3. Schematic representation of the bending actuation of CNa/GO films exposed to asymmetrical moisture (a). Images of humidity-driven bending actuation of CNa/GO 50/50 at different times, from ~1 s to 5 days (b1-8). Diagram of the bending kinetics of CNa/GO 50/50 (c). Graphical representation of the water gradient kinetics in a CNa/GO film section asymmetrically exposed to moisture (d). Images of CNa/GO 50/50 film exposed to humidity with both sides of the film, alternately (e1-6).

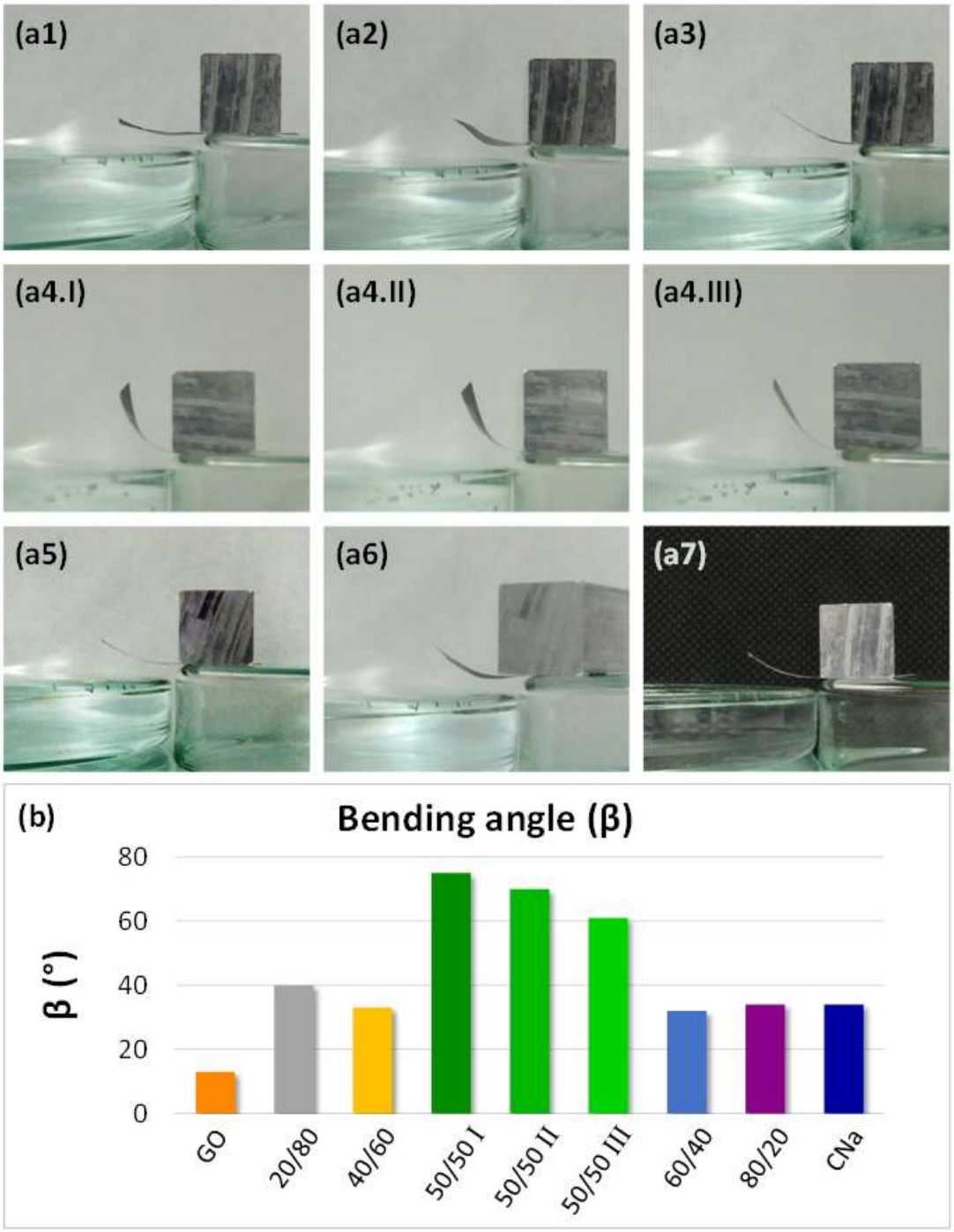

Figure 4. Images of humidity-driven bending actuation of: GO (a1), CNa/GO 20/80 (a2), CNa/GO 40/60 (a3), CNa/GO 50/50 during three consecutive moisture exposure cycles (a4.I, a4.II, a4.III), CNa/GO 60/40 (a5), CNa/GO 80/20 (a6) and CNa (a7). Diagram of first-response bending angles (β) of GO, CNa and CNa/GO hybrid films asymmetrically exposed to moisture (b).

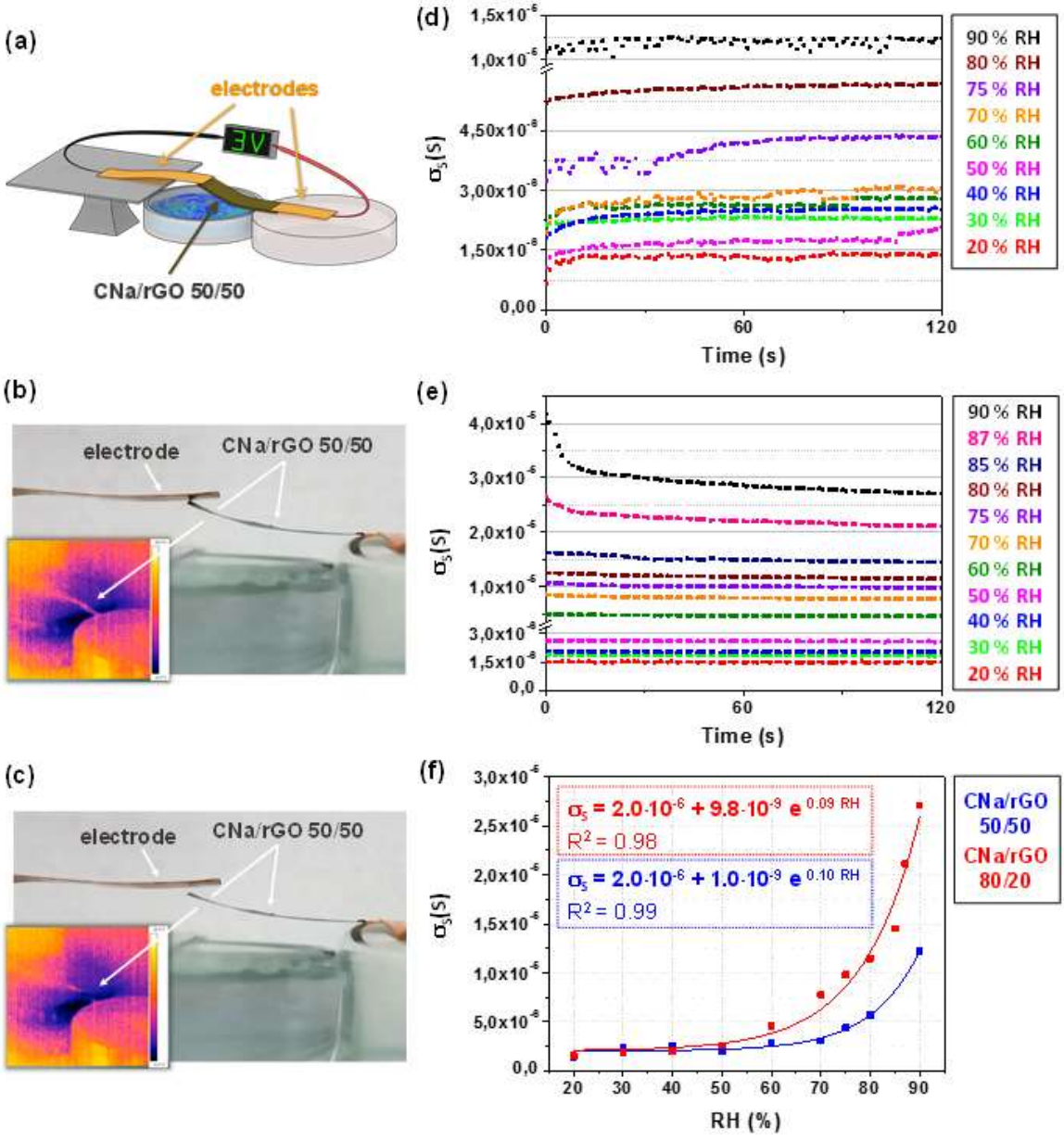

Figure 5. Schematic representation (a) and images of CNa/rGO 50/50 humidity and electricity driven actuation and sensing test showing the closed (b) and open circuit (c); thermal camera images are shown in insets. Surface conductivity (σ_S) of CNa/rGO 50/50 (d), and CNa/rGO 80/20 (e) films at different RH values. Stationary values of CNa/rGO 50/50 and CNa/rGO 80/20 surface conductivity at variable RH are reported in (f), with curves resulting from their exponential fit.

Table 1. XRD, tensile test and water contact angle (CA) results of GO, CNa and hybrids films, and the corresponding thermally reduced samples.

Sample	XRD						Tensile tests			CA [°]
	$2\theta_1$ [°]	d_1 [nm]	D_1 [a] [nm]	$2\theta_2$ [°]	d_2 [nm]	D_2 [a] [nm]	E [GPa]	σ [GPa]	ε [%]	
GO				10.74	0.823	11.37	7.9 ± 0.1	3.5 ± 0.1	0.67 ± 0.15	73 ± 6
CNa/GO 50/50	7.30	1.21	4.53	10.21	0.865	6.18	6.1 ± 0.2	4.6 ± 0.2	1.47 ± 0.20	39 ± 3
CNa/GO 80/20	7.21	1.23	6.92	10.24	0.863	12.02	5.7 ± 0.2	5.8 ± 0.2	1.53 ± 0.17	37 ± 5
CNa	7.38	1.20	8.16	-	-	-	3.7 ± 0.1	2.5 ± 0.1	0.74 ± 0.08	50 ± 11
rGO	-	-	-	23.37	0.380	1.41	0.5 ± 0.1	0.5 ± 0.1	0.78 ± 0.07	80 ± 8
CNa/rGO 50/50	7.34	1.20	3.15	15.02	0.589	-	2.1 ± 0.1	2.2 ± 0.1	1.16 ± 0.12	82 ± 7
CNa/rGO 80/20	7.40	1.19	3.43	17.71	0.500	-	4.1 ± 0.2	2.9 ± 0.1	2.92 ± 0.31	81 ± 5

a) Di = mean size of the stacked GO and cloisite domains in the direction perpendicular to the film surface, calculated from the reflection i

Facile preparation of graphene oxide/cloisite hybrid films results in new humidity-driven mechanically and electrically responsive actuators and sensors. Hybrids show humidity-triggered bidirectional bending whose extent is tuned by tailoring the graphene oxide/cloisite ratio. By thermal treatment, reduced graphene oxide/cloisite hybrids are obtained, which show moisture-dependent electrical conductivity and generate contractile/relaxation stress upon humidity changes.

Keywords: graphene/cloisite hybrids, reversible bending, humidity sensing, humidity-triggered actuators

R. Castaldo, G. C. Lama, P. Aprea, G. Gentile*, V. Ambrogi*, M. Lavorgna, P. Cerruti

Humidity-driven mechanical and electrical response of graphene/cloisite hybrid films